

Element Stratification in the Middle-aged SN Ia Remnant G344.7–0.1

KOTARO FUKUSHIMA,¹ HIROYA YAMAGUCHI,^{2,3} PATRICK O. SLANE,⁴ SANGWOOK PARK,⁵ SATORU KATSUDA,⁶ HIDETOSHI SANO,^{7,8}
LAURA A. LOPEZ,^{9,10,11} PAUL P. PLUCINSKY,⁴ SHOGO B. KOBAYASHI,¹ KYOKO MATSUSHITA,¹

¹*Department of Physics, Tokyo University of Science, 1-3 Kagurazaka, Shinjuku-ku, Tokyo 162-8601, Japan*

²*Institute of Space and Astronautical Science, JAXA, 3-1-1 Yoshinodai, Sagami-hara, Kanagawa 229-8510, Japan*

³*Department of Physics, The University of Tokyo, 7-3-1 Hongo, Bunkyo-ku, Tokyo 113-0033, Japan*

⁴*Harvard-Smithsonian Center for Astrophysics, 60 Garden Street, Cambridge, MA 02138, USA*

⁵*Box 19059, Department of Physics, University of Texas at Arlington, Arlington, TX 76019, USA*

⁶*Graduate School of Science and Engineering, Saitama University, 255 Shimo-Ohkubo, Sakura, Saitama 338-8570, Japan*

⁷*Institute for Advanced Research, Nagoya University, Furo-cho, Chikusa-ku, Nagoya 464-8601, Japan*

⁸*Department of Physics, Nagoya University, Furo-cho, Chikusa-ku, Nagoya 464-8601, Japan*

⁹*Department of Astronomy, The Ohio State University, 140 W. 18th Avenue, Columbus, Ohio 43210, USA*

¹⁰*Center for Cosmology and AstroParticle Physics, The Ohio State University, 191 W. Woodruff Avenue, Columbus, OH 43210, USA*

¹¹*Niels Bohr Institute, University of Copenhagen, Blegdamsvej 17, DK-2100 Copenhagen, Denmark*

(Received February 11, 2020; Revised May 10, 2020; Accepted May 17, 2020)

Submitted to *Astrophysical Journal*

ABSTRACT

Despite their importance, a detailed understanding of Type Ia supernovae (SNe Ia) remains elusive. X-ray measurements of the element distributions in supernova remnants (SNRs) offer important clues for understanding the explosion and nucleosynthesis mechanisms for SNe Ia. However, it is challenging to observe the entire ejecta mass in X-rays for young SNRs, because the central ejecta may not have been heated by the reverse shock yet. Here we present over 200 kilosecond Chandra observations of the Type Ia SNR G344.7–0.1, whose age is old enough for the reverse shock to have reached the SNR center, providing an opportunity to investigate the distribution of the entire ejecta mass. We reveal a clear stratification of heavy elements with a centrally peaked distribution of the Fe ejecta surrounded by intermediate-mass elements (IMEs: Si, S, Ar Ca) with an arc-like structure. The centroid energy of the Fe K emission is marginally lower in the central Fe-rich region than in the outer IME-rich regions, suggesting that the Fe ejecta were shock-heated more recently. These results are consistent with the prediction for standard SN Ia models, where the heavier elements are synthesized in the interior of an exploding white dwarf. We find, however, that the peak location of the Fe K emission is slightly offset to the west with respect to the geometric center of the SNR. This apparent asymmetry is likely due to the inhomogeneous density distribution of the ambient medium, consistent with our radio observations of the ambient molecular and neutral gas.

Keywords: ISM: individual objects (G344.7–0.1) – ISM: supernova remnants – X-rays: ISM

1. INTRODUCTION

Type Ia supernovae (SNe Ia) are thought to result from thermonuclear explosions of white dwarfs in a binary system. Since the peak luminosity in the optical band is almost uniform among the objects, SNe Ia can be utilized as distance indicators in cosmology (e.g., [Riess et al. 1998](#); [Perlmutter et al. 1998](#)). SNe Ia also play an important role as major suppliers of iron, contributing to the chemical enrichment of the Milky Way (e.g., [Reddy et al. 2006](#)) and galaxy clusters (e.g., [Sato et al. 2007](#)). Despite this impor-

tance, however, many fundamental aspects of these explosions remain elusive.

X-ray observations of supernova remnants (SNRs) offer a unique way to address the relevant open questions, as they allow us to measure the composition and distribution of heavy elements that were synthesized during the SN explosion. In fact, recent observational studies of young, luminous Type Ia SNRs, such as Kepler, Tycho, and SN 1006, have provided important insights into the evolution of the explosions of their progenitors (e.g., [Vink 2017](#); [Decourchelle 2017](#); [Katsuda 2017](#), and references therein). In these young his-

Table 1. Observation Log

Obs. ID	Date	Exposure Time(ks)	Aim Point ^a	Roll Angle
20308	2018 May 16	29.2	255°.99, −41°.72	50°.21
20309	2018 May 12	55.3	255°.99, −41°.72	51°.21
21093	2018 May 18	33.6	255°.99, −41°.72	50°.21
21094	2018 May 19	14.9	255°.99, −41°.72	50°.21
21095	2018 May 20	26.7	255°.99, −41°.72	50°.21
21096	2018 Jul 3	27.2	256°.06, −41°.71	303°.2
21117	2018 Jul 5	18.8	256°.06, −41°.71	303°.2

^aIn the (R.A., decl.)_{J2000} coordinate.

torical SNRs, however, the central ejecta might not yet have been heated by the reverse shock and thus are invisible in X-rays. Thus, while some extensive studies have been performed with these young Ia SNRs, our knowledge of how the SN Ia explosion begins or what happens in the deepest layers of the exploding white dwarf is still limited.

The Type Ia SNR G344.7−0.1 is an ideal target for a comprehensive X-ray ejecta study of SN Ia, because its age is significantly older (3–6 kyr: [Combi et al. 2010](#); [Giacani et al. 2011](#)) than the historical Ia SNRs, for which the reverse shock has likely reached the SNR center. This SNR was discovered in the radio band with the Molonglo Observatory Synthesis Telescope (MOST) and the Parkes Observatory ([Clark et al. 1975](#)). X-rays from this region were first detected by the ASCA Galactic Plane Survey ([Sugizaki et al. 2001](#)), and identified as emission originating from an optically thin thermal plasma associated with the SNR ([Yamauchi et al. 2005](#)). The following studies with Chandra and XMM-Newton enabled more detailed imaging and spectroscopic analysis, where the abovementioned SNR ionization age was estimated ([Combi et al. 2010](#); [Giacani et al. 2011](#)). G344.7−0.1 was initially classified as a core-collapse (CC) SNR, based on its highly asymmetric X-ray morphology ([Lopez et al. 2011](#)) and possible association with star forming regions ([Giacani et al. 2011](#)). However, elemental abundances of the SN ejecta were not well constrained in these studies, mainly due to the short exposure, ~ 25 ks for both Chandra and XMM-Newton.

The situation was largely changed by Suzaku observations, where strong, ejecta-dominated Fe K emission was detected ([Yamaguchi et al. 2012](#)). Its centroid energy ~ 6.46 keV corresponds to a relatively low ionization state (Fe^{17+}), which is proposed to be a common characteristic for Type Ia SNRs ([Yamaguchi et al. 2014a](#)). Notably, the atomic processes involved in the Fe K fluorescence emission are theoretically well understood (e.g., [Yamaguchi et al. 2014b](#)). Thus, the detection of the Fe K emission from this SNR is a remarkable advantage compared to other Type Ia SNRs (with sim-

ilar ages of several kyr, e.g., G299.2−2.9: [Post et al. 2014](#); DEM L71: [Hughes et al. 2003](#)), where the X-ray spectra are dominated by Fe L-shell emission with highly uncertain atomic physics. Unfortunately, the angular resolution of Suzaku was not good enough to constrain the detailed distribution of the Fe ejecta in G344.7−0.1. This motivated us to carry out deep Chandra observations to reveal the distribution of the entire SN ejecta mass, including Fe, the major nucleosynthesis product of SNe Ia.

It should also be noted that the previous Chandra observation detected a point-like source in the soft X-ray band, named CXOU J170357.8−414302, at the geometrical center of G344.7−0.1 ([Combi et al. 2010](#)). Since the absorption column density of this source ($N_{\text{H}} \approx 1 \times 10^{22} \text{ cm}^{-2}$) was significantly lower than that of the SNR ($5 \times 10^{22} \text{ cm}^{-2}$), it was concluded in their work that the source was a foreground object unassociated with the SNR. However, one may still suspect the possibility of a central compact object (CCO) originating from a CC progenitor, because of the poor photon statistics from the previous observation. Our additional 200 ks Chandra observations also allow us to confirm that this object is unrelated to G344.7−0.1 with better statistics and to search for other point-like sources near the SNR center.

In Section 2, we describe details of our Chandra observations and data reduction. In Section 3, we present our imaging and spectral analysis. We discuss the results in Section 4 and present our conclusions in Section 5. The errors quoted in this work are at 1σ confidence level, unless otherwise stated.

2. OBSERVATIONS AND DATA REDUCTION

We used the ACIS-I array ([Garmire et al. 2003](#)) for our deep observations of G344.7−0.1 to cover the whole X-ray emitting region ($\sim 8'$ in diameter) within a single field of view (FoV). The ACIS-I has a lower background level than the S3 chip, especially at energies above 5 keV, offering a great advantage for our primary objective: detection and localization of the Fe K emission.

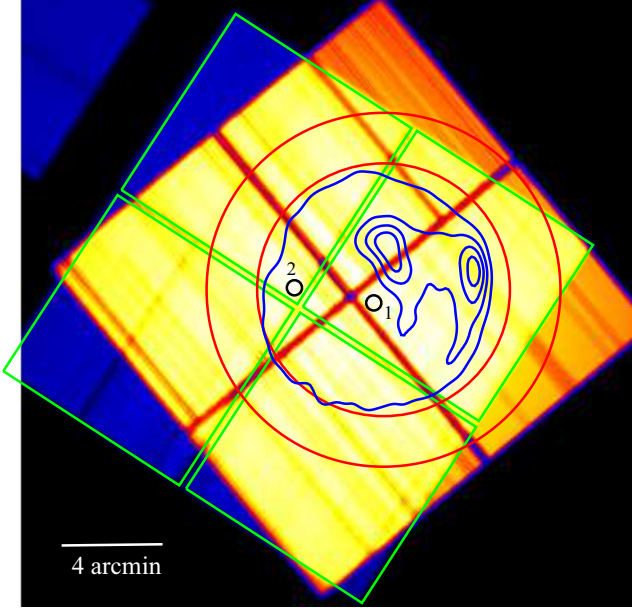


Figure 1. Merged exposure map of our deep *Chandra* observations presented in this paper. The maps from the two observation series are combined (see the text for the details). The green squares indicate the ACIS-I FoV of the shorter (~ 45 ks) observation series in 2018 July. The black circles labeled 1 and 2 indicate the on-axis aim points of the former and latter observations, respectively. The red annulus is the background region used for the spectral analysis. The blue contours are the 843 MHz radio image of G344.7–0.1 taken from the MOST Supernova Remnant Catalog (Whiteoak & Green 1996). North is up and east is to the left.

As summarized in Table 1, the observations were split into two series, one in May and the other in 2018 July, with the exposure totaling ~ 205 ks. Our quick-look analysis after the first observations series revealed that the Fe K emission partially fell into the gaps between the ACIS-I CCDs, where the exposure is reduced as shown in Figure 1. Therefore, we slightly shifted the aim point for the later observation series such that the Fe-rich regions received the maximum exposure. The difference in the aim points and roll angles between the two series is indicated in Figure 1 with the integrated exposure map overplotted with the radio intensity contours of the SNR.

We reprocess the data in accordance with the standard reduction procedures using CIAO version 4.11 (Fruscione et al. 2006) and the calibration database (CALDB) version 4.8.2. For spectral analysis presented in §3.2, and Appendix A, we extract ACIS spectra and generated RMFs and ARFs for each individual ObsID, and those taken in the same observation series (i.e., May or July) are summed up to improve the photon statistics. The two merged

spectra taken from the same sky regions but different series are jointly fitted with the identical spectral parameters.

3. ANALYSIS AND RESULTS

3.1. Imaging Analysis

3.1.1. Extended Emission

Figure 2(a) shows a three-color, exposure-corrected image of G344.7–0.1, where red, green, and blue correspond to emission from the Si K (1.76–1.94 keV), hard continuum (3.0–6.0 keV), and Fe K (6.35–6.55 keV) band, respectively. The image indicates that the softer X-ray emission (red) spreads across the entire SNR, whereas the hard X-ray continuum (green) is relatively faint in the northeast region, implying a temperature gradient from the southwest (high) to the northeast (low). This gradient is more clearly highlighted in Figure 2(b), a map of the mean energy of the detected photons in the broad energy band of 1.5–5.0 keV generated using the `mean_energy_map` script in the CIAO package.¹ Note, however, that this energy band includes several emission lines, and thus a more quantitative spectral analysis (§3.2) is required to determine the accurate temperature distribution.

Figures 2(c) and (d) are the narrowband images of the Si K and Fe K emission, identical to the red and blue images in Figure 2(a) respectively. It is remarkable that the Fe K line-enhanced region is surrounded by the arc-like structure of the Si K emission. Also notable is that the Fe K peak location is about $2'$ offset to the west with respect to the geometric center of the SNR determined by the radio band image. In addition to the arc of the Si K emission, a filamentary structure is found at the west rim in the same energy band, indicated with the dashed ellipse in Figure 2(c). All of these features are discovered in this work for the first time, owing to the deep observations with the Chandra ACIS-I.

We generate in Figure 3 radial profiles of the surface brightness in the narrow energy bands that correspond to the K-shell emission of Si (1.76–1.94 keV), S (2.25–2.60 keV), Ar (2.95–3.25 keV), Ca (3.60–4.10 keV), and Fe (6.35–6.55 keV). We confirm that the Fe K emission profile indeed peaks at the interior to other species. We also find that the profiles of the intermediate-mass elements (IMEs) are similar to each other.

3.1.2. Detected Point-like Sources

Figure 2(e) shows a 0.5–1.2 keV image of the same region as the other panels of Figure 2. Because of the

¹ The mean photon energy (MPE) is defined as $\langle E(x, y) \rangle = (\sum_i E_i(x, y)) / N(x, y)$ (where E_i and N are the energy of each photon and the total number of photons detected in the pixel x, y). An MPE map is known to represent the temperature distribution, when the photons are extracted from the broad energy band (e.g., Troja et al. 2008; David et al. 2009).

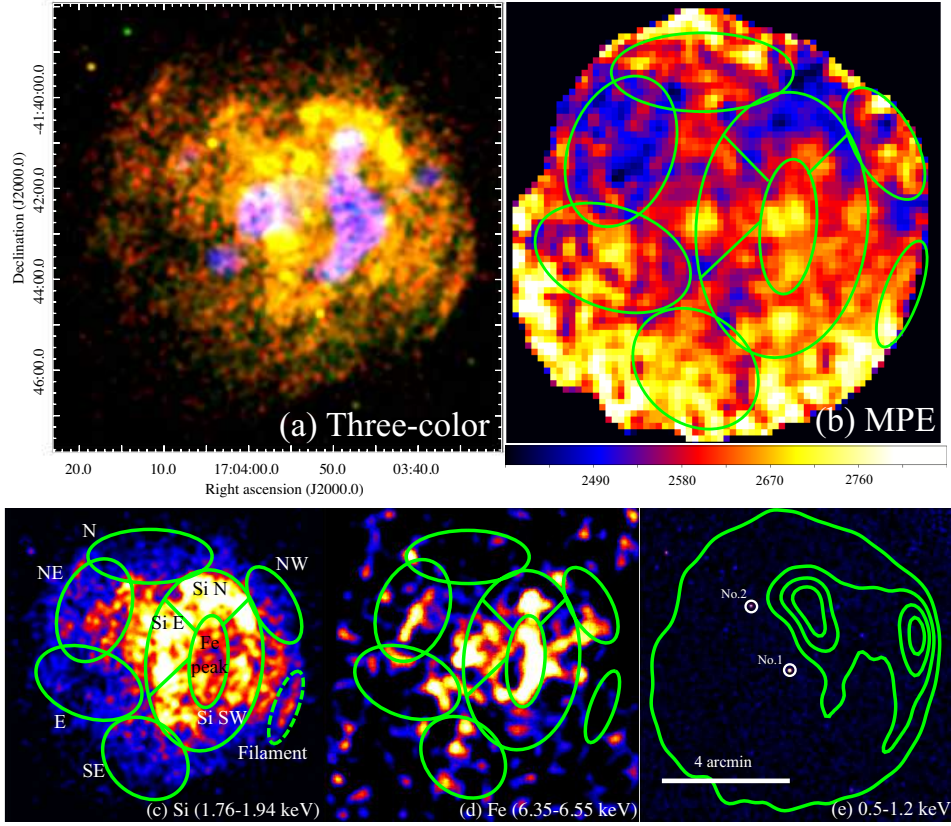


Figure 2. ACIS-I images of G344.7–0.1. (a) Three-color image, where red, green, and blue correspond to emission from the Si K (1.76–1.94 keV), hard continuum (3.0–6.0 keV), and Fe K (6.35–6.55 keV) bands, respectively. (b) Mean energies of the 1.5–5.0 keV photons. The color bar is in units of eV. The spectrum extraction regions are indicated by the green ellipses. (c) and (d) Narrowband images in the 1.76–1.94 keV and 6.35–6.55 keV bands, corresponding to the Si K and Fe K emission. (e) Soft X-ray image in the 0.5–1.2 keV band. The radio image of the SNR is overlaid in contours. Two bright point-like sources are identified.

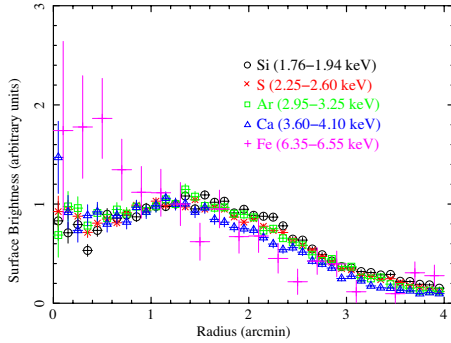


Figure 3. Radial profiles of the surface brightness in the K-shell emission bands of Si, S, Ar, Ca, and Fe, where the continuum flux is unsubtracted. The Fe peak position shown in Figure 2 is taken as the origin of these profiles. Surface brightness is extracted from the exposure-corrected flux images of the corresponding energy bands and then linearly scaled so that the normalization of the bin at $r = 1'.35$ becomes unity for each element.

large foreground extinction ($N_{\text{H}} \sim 5 \times 10^{22} \text{ cm}^{-2}$; Yamauchi et al. 2005; Combi et al. 2010; Giacani et al. 2011; Yamaguchi et al. 2012), soft X-rays from G344.7–0.1 are almost fully absorbed. Therefore, photons in this energy band are likely dominated by foreground objects. Our simple eyeball inspection detects the two bright point-like sources, labeled No.1 and 2 in Figure 2(e). Source No.1 corresponds to CXOU J170357.8–414302, previously reported by Combi et al. (2010). This source is located near the geometric center of the SNR, and does not positionally coincide with the Fe K peak location. The other (No.2) is newly detected with our deep Chandra observation. We also search for fainter point sources using the wavdetect algorithm in the two energy ranges of 0.5–1.2 keV and 1.2–2.5 keV with the Encircled Counts Fraction (ECF) parameter set to 0.9. Table 2 gives the detected sources with their coordinates, spatial extent relative to the size of the point spread function (PSFRATIO), and the counts in the 0.5–2.0 keV (soft) and 2.0–9.0 keV (hard) bands. We regard those with PSFRATIO

Table 2. List of the Detected Point-like Sources

No.	(R.A., decl) _{J2000}	PSFRATIO ^a	Soft ^b	Hard ^c	No.	(R.A., decl) _{J2000}	PSFRATIO ^a	Soft ^b	Hard ^c
1	17 : 03 : 57.8, −41 : 43 : 02.2	0.56	146	44	26	17 : 03 : 36.8, −41 : 40 : 46.5	0.35	29	65
2	17 : 04 : 04.3, −41 : 41 : 01.0	0.48	114	38	27	17 : 03 : 54.4, −41 : 40 : 19.9	0.70	31	59
3	17 : 03 : 47.5, −41 : 46 : 47.1	0.77	65	67	28	17 : 04 : 09.3, −41 : 40 : 11.3	0.69	22	29
4	17 : 04 : 04.1, −41 : 45 : 36.2	0.24	24	2	29	17 : 04 : 19.3, −41 : 38 : 56.3	0.84	29	85
5	17 : 04 : 01.2, −41 : 43 : 35.6	0.25	8	2	30	17 : 03 : 55.1, −41 : 46 : 33.7	0.90	56	110
6	17 : 03 : 53.4, −41 : 42 : 32.2	0.34	35	27	31	17 : 03 : 53.9, −41 : 41 : 33.3	0.62	36	80
7	17 : 03 : 45.7, −41 : 41 : 56.4	0.43	46	33	32	17 : 03 : 49.8, −41 : 41 : 01.8	0.81	78	128
8	17 : 04 : 09.1, −41 : 39 : 56.9	0.64	28	31	33	17 : 03 : 38.5, −41 : 45 : 15.2	0.64	41	124
9	17 : 04 : 07.0, −41 : 39 : 49.6	0.72	32	17	34	17 : 03 : 37.2, −41 : 44 : 36.8	0.80	137	306
10	17 : 04 : 11.8, −41 : 39 : 31.0	0.33	17	1	35	17 : 03 : 52.7, −41 : 44 : 27.8	0.51	20	32
11	17 : 03 : 41.6, −41 : 46 : 28.9	0.47	21	39	36	17 : 03 : 35.9, −41 : 44 : 22.0	0.51	49	118
12	17 : 04 : 03.0, −41 : 44 : 06.2	0.28	8	3	37	17 : 03 : 46.8, −41 : 44 : 13.8	0.68	39	109
13	17 : 04 : 11.7, −41 : 39 : 53.4	0.28	11	4	38	17 : 03 : 44.7, −41 : 43 : 57.6	0.37	15	34
14	17 : 04 : 20.1, −41 : 39 : 47.7	0.35	28	13	39	17 : 03 : 34.4, −41 : 43 : 20.2	0.67	80	170
15	17 : 04 : 18.5, −41 : 39 : 21.0	0.38	46	22	40	17 : 03 : 55.2, −41 : 43 : 12.4	0.30	7	7
16	17 : 04 : 16.3, −41 : 38 : 37.9	0.36	24	7	41	17 : 03 : 56.1, −41 : 43 : 00.6	0.38	10	20
17	17 : 04 : 14.4, −41 : 38 : 34.2	0.62	80	70	42	17 : 03 : 43.9, −41 : 42 : 43.3	0.48	25	57
18	17 : 03 : 38.8, −41 : 46 : 36.1	0.45	40	38	43	17 : 03 : 37.0, −41 : 42 : 20.0	0.76	116	191
19	17 : 03 : 36.8, −41 : 39 : 40.1	0.55	35	44	44	17 : 04 : 00.3, −41 : 42 : 07.1	0.51	8	14
20	17 : 03 : 51.7, −41 : 44 : 45.8	0.95	118	187	45	17 : 03 : 46.1, −41 : 40 : 52.3	0.24	14	20
21	17 : 04 : 04.7, −41 : 43 : 47.9	0.39	15	9	46	17 : 03 : 43.4, −41 : 40 : 55.5	0.60	70	130
22	17 : 04 : 02.3, −41 : 46 : 23.0	0.60	39	39	47	17 : 03 : 50.4, −41 : 40 : 16.8	0.90	105	160
23	17 : 04 : 19.7, −41 : 42 : 52.4	0.43	19	10	48	17 : 04 : 11.1, −41 : 40 : 01.8	0.91	51	69
24	17 : 03 : 33.9, −41 : 45 : 49.8	0.60	68	108	49	17 : 03 : 53.4, −41 : 38 : 37.4	0.91	41	130
25	17 : 04 : 14.0, −41 : 41 : 28.7	0.79	22	31					

^a A parameter of `wavdetect` that indicates the spatial extension of the sources with respect to the PSF size. The source can be regarded as a true point source when this value is the unity or less.

^b Photon counts in 0.5–2.0 keV.

^c Photon counts in 2.0–9.0 keV.

< 1 as true point sources. About 50 sources are detected based on these criteria.

3.2. Spectral Analysis

3.2.1. Extended Emission

Here we analyze ACIS-I spectra extracted from the regions given in Figure 2, where the point sources detected in the previous section (Table 2) are excluded. In our analysis we model the background emission instead of subtracting it. Figure 4 shows the spectra of several representative regions, where black and red are the data from the May and July observations, respectively. The emission lines of the IMEs and Fe are clearly resolved in each region. Background data are extracted from an annulus region surrounding the SNR with inner and outer radii of 5'.0 and 7'.0, respectively (Figure 1). We model and fit the background spectra simulta-

neously with the source spectra, instead of subtracting them from the source data, to properly take into account the difference in the effective area between the source and background regions. The details of the background spectral modeling are presented in Appendix A. In the following spectral analysis, we fit unbinned data using the C-statistics (Cash 1979) to estimate the model parameters and their error ranges without bias, although the binned spectra are shown in the figures for clarity.

We first fit the spectra with a model of an optically thin thermal plasma in the non-equilibrium ionization (NEI) state, i.e., the `vnei` model in the XSPEC package, based on the latest atomic database (AtomDB² version 3.0.9). We use the

² <http://www.atomdb.org>

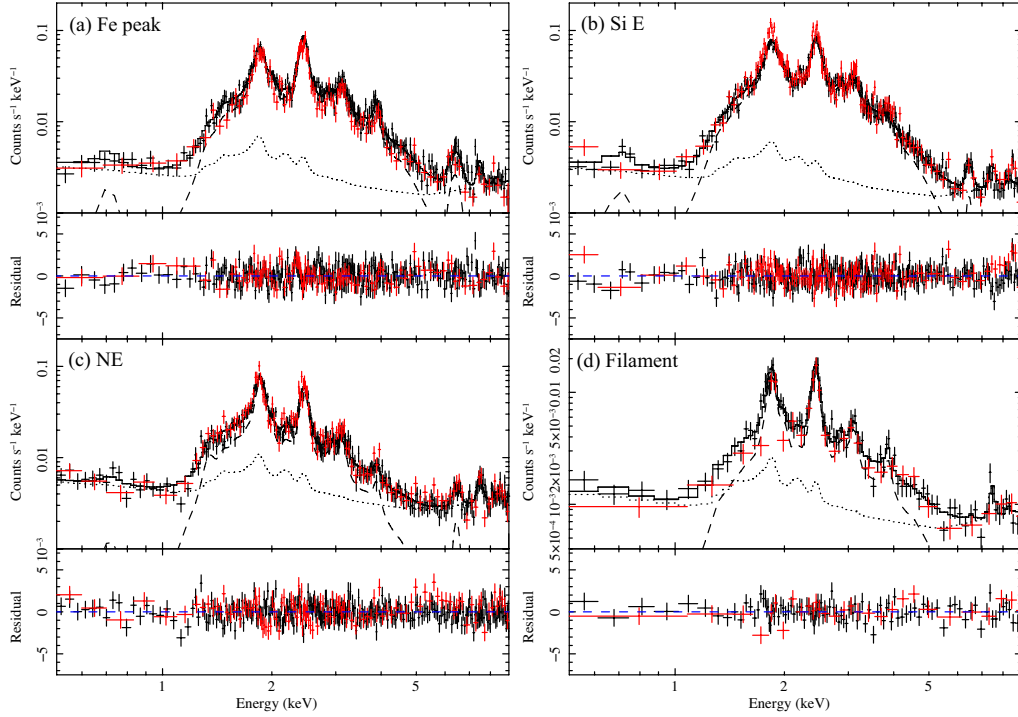


Figure 4. Spectra of representative regions: (a) Fe peak, (b) Si E, (c) NE, and (d) Filament defined in Figure 2. The black and red data are the data from the May and July observation series, respectively. The dashed lines represent the NEI component and Fe K emission in the best-fit models for the spectrum taken in 2018 May, whereas the dotted lines represent the modeled background components.

tbnew_gas model³ for the foreground absorption, assuming the photoelectric absorption cross sections taken from Verner et al. (1996). The free parameters are the absorption column density N_H , electron temperature kT_e , ionization timescale $n_e t$, volume emission measure (VEM), and elemental abundances of Mg, Si, S, Ar, Ca, and Fe relative to the solar abundance table of Wilms et al. (2000). This model gives good fits to the spectra below 5 keV, but fails to reproduce the Fe K emission. We find that the model generally predicts an Fe K centroid energy higher than the observed values, which indicates that the Fe K emission originates from another plasma component with a lower ionization state.

We thus add a Gaussian component to reproduce the K-shell emission from the low-ionized Fe. The addition of this component significantly improves the fit, with the C-stat value reduced from 1003.00/805 to 920.43/803 in the 5.0–8.0 keV band, including the strong Fe K line. The best-fit model spectra and parameters are given in Figure 4 and Table 3, respectively. The abundances of the IMEs (but for Mg) are generally higher than the solar values, implying a significant ejecta contribution to the vnei component. We also

find that both the electron temperature (of the vnei component) and the Fe K centroid energy vary among the regions. The lowest temperature is observed in the N and NE, consistent with the mean photon energy map (Figure 2b). The Fe K centroid energy is marginally lower in the Fe peak region than in most of the outer regions, indicating that the Fe ejecta in the former has a low ionization degree. The absorption column density is found to be almost uniform throughout the SNR, $\sim 6.5 \times 10^{22} \text{ cm}^{-2}$. This value is slightly higher than the previous measurements of $N_H = 4.0\text{--}5.5 \times 10^{22} \text{ cm}^{-2}$ (Yamauchi et al. 2005; Combi et al. 2010; Giacani et al. 2011; Yamaguchi et al. 2012). This discrepancy is likely due to the difference in the reference solar abundance; the previous work referred to Anders & Grevesse (1989), while we refer to Wilms et al. (2000). In fact, if we fit the ACIS-I spectra using the solar abundance table of Anders & Grevesse (1989), we obtain $N_H \sim 4.5 \times 10^{22} \text{ cm}^{-2}$, consistent with the previous work.

Next, we replace the Gaussian component with another vnei component to account for the emission from pure Fe ejecta. The SNR is now divided into three regions, the Fe peak, Si-arc (containing Si E, N, and SW), and rim (containing N, NE, NW, SE, S, and Filament), and their spectra are jointly fitted with a common N_H value. Table 4 gives the parameter values obtained for the pure Fe ejecta com-

³ <https://pulsar.sternwarte.uni-erlangen.de/wilms/research/tbabs/>

Table 3. Best-fit Spectral Parameters for the Extended Emission

Components	Parameters	Fe	Si N	Si E	Si SW	N
Absorption ^a	N_H (10^{22} cm ⁻²)	$6.40^{+0.34}_{-0.24}$	$6.68^{+0.29}_{-0.29}$	$6.47^{+0.22}_{-0.20}$	$6.52^{+0.18}_{-0.17}$	$6.28^{+0.48}_{-0.50}$
NEI plasma ^b	kT_e (keV)	$1.10^{+0.04}_{-0.08}$	$0.83^{+0.05}_{-0.04}$	$0.93^{+0.03}_{-0.03}$	$0.99^{+0.03}_{-0.03}$	$0.81^{+0.08}_{-0.07}$
	Mg	$0.45^{+0.33}_{-0.24}$	$1.14^{+0.40}_{-0.31}$	$0.33^{+0.23}_{-0.19}$	$0.63^{+0.21}_{-0.18}$	$1.11^{+1.16}_{-0.60}$
	Si	$1.51^{+0.15}_{-0.16}$	$1.42^{+0.14}_{-0.12}$	$1.13^{+0.10}_{-0.09}$	$1.48^{+0.10}_{-0.09}$	$1.87^{+0.45}_{-0.17}$
	S	$2.28^{+0.15}_{-0.17}$	$1.69^{+0.11}_{-0.11}$	$1.49^{+0.09}_{-0.09}$	$2.03^{+0.09}_{-0.08}$	$2.13^{+0.27}_{-0.23}$
	Ar	$2.05^{+0.26}_{-0.24}$	$2.18^{+0.29}_{-0.27}$	$1.62^{+0.20}_{-0.19}$	$2.14^{+0.16}_{-0.16}$	$1.71^{+0.54}_{-0.49}$
	Ca	$4.26^{+0.58}_{-0.54}$	$4.09^{+1.22}_{-0.96}$	$1.85^{+0.44}_{-0.41}$	$4.41^{+0.49}_{-0.47}$	$1.82^{+2.05}_{-1.61}$
	n_{et} (10^{11} s cm ⁻³)	$1.74^{+0.49}_{-0.36}$	$1.48^{+0.37}_{-0.31}$	$2.17^{+0.45}_{-0.38}$	$1.49^{+0.21}_{-0.16}$	$1.67^{+0.85}_{-0.63}$
	VEM ^c	$8.22^{+1.87}_{-0.84}$	$18.9^{+3.2}_{-2.9}$	$17.5^{+1.8}_{-1.7}$	$26.5^{+2.4}_{-2.4}$	$5.90^{+1.96}_{-1.40}$
Fe K	E (keV)	$6.41^{+0.03}_{-0.03}$	$6.48^{+0.06}_{-0.06}$	$6.45^{+0.03}_{-0.03}$	$6.40^{+0.03}_{-0.03}$	$6.54^{+0.07}_{-0.07}$
	σ (eV)	206^{+35}_{-31}	100 (fix)	< 93	85^{+39}_{-40}	100 (fix)
	Flux ^d	$9.80^{+1.1}_{-1.1}$	$1.65^{+0.65}_{-0.62}$	$3.53^{+0.70}_{-0.66}$	$6.77^{+1.16}_{-1.07}$	$1.02^{+0.75}_{-0.68}$
Photon Counts (10^4 conut)		1.75	1.83	2.05	4.22	1.24
Background Contribution (%)		18.4	19.1	16.4	21.4	48.8
C-stat		2658.68	2690.62	2636.78	2739.07	2655.14
dof		2311	2312	2311	2311	2312
		NE	NW	E	SE	Filament
Absorption ^a	N_H (10^{22} cm ⁻²)	$6.19^{+0.31}_{-0.29}$	$5.30^{+0.75}_{-0.54}$	$6.63^{+0.60}_{-0.43}$	$6.69^{+0.57}_{-0.53}$	$5.80^{+0.84}_{-0.47}$
NEI plasma ^b	kT_e (keV)	$0.79^{+0.07}_{-0.05}$	$1.27^{+0.25}_{-0.25}$	$0.88^{+0.06}_{-0.10}$	$0.90^{+0.07}_{-0.07}$	$1.41^{+0.24}_{-0.21}$
	Mg	$1.25^{+0.49}_{-0.36}$	< 1.70	$1.18^{+0.81}_{-0.55}$	$0.66^{+0.70}_{-0.47}$	< 1.23
	Si	$2.09^{+0.27}_{-0.22}$	$3.03^{+0.89}_{-0.76}$	$1.87^{+0.34}_{-0.28}$	$1.61^{+0.31}_{-0.25}$	$2.22^{+0.73}_{-0.47}$
	S	$2.00^{+0.17}_{-0.15}$	$4.07^{+0.86}_{-0.80}$	$2.49^{+0.27}_{-0.25}$	$2.60^{+0.28}_{-0.24}$	$2.67^{+0.53}_{-0.43}$
	Ar	$2.83^{+0.46}_{-0.40}$	$3.72^{+1.03}_{-0.90}$	$2.74^{+0.51}_{-0.47}$	$3.16^{+0.48}_{-0.42}$	$2.15^{+0.73}_{-0.64}$
	Ca	$5.73^{+2.04}_{-1.61}$	$3.28^{+1.52}_{-1.30}$	$5.22^{+1.07}_{-0.84}$ ^e	$6.65^{+2.61}_{-1.58}$	$4.39^{+1.82}_{-1.46}$
	n_{et} (10^{11} s cm ⁻³)	$1.52^{+0.41}_{-0.35}$	$1.59^{+1.21}_{-0.47}$	$1.26^{+0.79}_{-0.33}$	$1.46^{+0.57}_{-0.43}$	$0.86^{+0.39}_{-0.23}$
	VEM ^c	$11.1^{+2.3}_{-2.2}$	$1.09^{+0.75}_{-0.35}$	$7.04^{+3.05}_{-1.28}$	$8.00^{+2.19}_{-1.76}$	$0.91^{+0.41}_{-0.25}$
Fe K	E (keV)	$6.45^{+0.03}_{-0.03}$	—	$6.46^{+0.03}_{-0.03}$ ^e	$6.46^{+0.03}_{-0.03}$ ^e	—
	σ (eV)	93.9^{+36}_{-35}	—	106^{+35}_{-36}	167^{+71}_{-58}	—
	Flux ^d	$5.22^{+0.94}_{-0.86}$	—	$5.31^{+1.10}_{-1.01}$	$3.88^{+1.10}_{-1.00}$	—
Photon Counts (10^4 conut)		3.73	0.69	1.48	1.52	0.40
Background Contribution (%)		35.5	45.6	46.5	40.6	35.8
C-stat		2704.56	2694.10	2601.55	2643.46	2671.64
dof		2311	2314	2313	2312	2314

^aThe absorption cross sections are taken from [Verner et al. \(1996\)](#).

^bSolar abundances of [Wilms et al. \(2000\)](#) are assumed.

^cIn units of 10^{11} cm⁻⁵. The volume emission measure (VEM) is given as $\int n_e n_H dV / (4\pi D^2)$, where V and D are the volume of the emission region (cm³) and the distance to the emitting source (cm), respectively.

^dIn units of 10^{-6} photon cm⁻² keV⁻¹ s⁻¹.

^eThese are determined using spectra extracted from a larger region containing both E and SE, since the values cannot be constrained for each individual region.

ponent. We find that the temperature of this component ($kT_e > 2.8$ keV) is significantly hotter than that of the IME component ($kT_e = 0.8$ – 1.1 keV). We also find that n_{et} of the

Fe ejecta $< 2 \times 10^{10}$ s cm⁻³ is lower than that of the IME component $\sim 2 \times 10^{11}$ s cm⁻³, and that the lowest n_{et} of the Fe ejecta component is achieved at the Fe peak region.

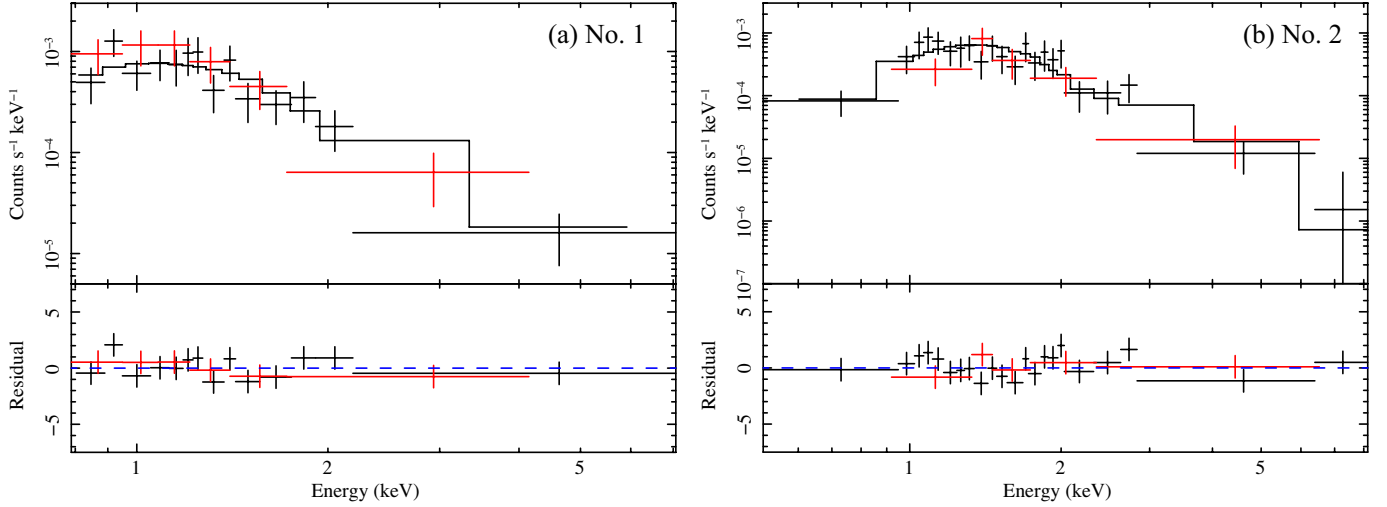


Figure 5. Background-subtracted spectra of the source of (a) No. 1 and (b) No. 2. The black and red data are the data from the May and July observation series, respectively. The solid line represents the best-fit power-law model for the former spectrum.

Table 4. Best-fit Spectral Parameters for the pure Fe Component

Parameters	Fe Peak	Si-arc	Rim
kT_e (keV)	$2.9^{+0.1}_{-0.1}$	$5.6^{+5.6}_{-0.4}$	$3.8^{+0.2}_{-0.2}$
$n_e t$ (10^9 s cm^{-3})	< 0.14	$3.5^{+1.8}_{-1.8}$	$17.4^{+2.1}_{-2.2}$
VEM ^a (10^5 cm^{-5})	$1.2^{+0.1}_{-0.1}$	$0.8^{+0.4}_{-0.1}$	$2.3^{+0.1}_{-0.5}$

^aThe VEM is given as $\int n_e n_{\text{Fe}} dV / (4\pi D^2)$.

photon counts are analyzed as well, obtaining statistically acceptable results (C-stat/dof $\lesssim 1.2$) for all the sources. The results are discussed in more detail in §4.3.

Table 5. Best-fit spectral parameters for the bright point sources

No.	N_{H}^a	Γ	N_{H}^a	kT_{bb}^b	N_{H}^a	kT_{APEC}^b
1	< 0.08	$3.44^{+0.29}_{-0.24}$	< 0.06	$0.24^{+0.02}_{-0.01}$	$0.58^{+0.18}_{-0.18}$	$0.92^{+0.10}_{-0.14}$
2	$0.93^{+0.35}_{-0.31}$	$3.84^{+0.53}_{-0.47}$	< 0.16	$0.43^{+0.03}_{-0.03}$	$1.20^{+0.25}_{-0.50}$	$1.04^{+0.31}_{-0.15}$

^aIn units of 10^{22} cm^{-2} .

^bIn units of keV.

3.2.2. Point-like Sources

We perform spectral analysis of two bright sources (No. 1 and No. 2) detected in the soft X-ray band, both embedded in the diffuse emission from the SNR (Figure 2e). The spectra of source No. 1 (CXOU J170357.8–414302) and No. 2 are shown in Figure 5. We fit the spectra of both sources with the following three models: an absorbed power law (tbnew_gas \times powerlaw), an absorbed blackbody (tbnew_gas \times bbody), and an absorbed optically thin thermal plasma with the solar abundances (tbnew_gas \times apec). We use background spectra extracted from the annulus surrounding each source region. For source No. 1, we obtain 160 counts for the background-corrected spectrum with 16% background contribution, and 136 counts with 8.6% for No. 2. The best-fit parameters we obtain are given in Table 5. The estimated column densities are significantly lower than that of the SNR ($N_{\text{H}} \approx 6.5 \times 10^{22} \text{ cm}^{-2}$) for any model assumption, consistent with the foreground stellar object explanation as suggested by Combi et al. (2010) for No. 1. The spectra of the other detected sources (Table 2) with sufficient

4. DISCUSSION

4.1. Stratified Elemental Composition

Thanks to the deep observations with Chandra, we have revealed the centrally peaked Fe K emission surrounded by the arc-like structure of the IME emission. This radially stratified chemical composition with Fe at the interior is consistent with the standard picture of SN Ia nucleosynthesis dominated by the carbon detonation (e.g. Iwamoto et al. 1999; Seitenzahl et al. 2013). Several other SN Ia explosion models, such as those involving pure carbon deflagration (e.g. Fink et al. 2014) or He-shell detonation (e.g. Sim et al. 2012), predict a substantial amount of ^{56}Ni (which decays into Fe) synthesized outside of the IME. We do not find such evidence in the X-ray data of G344.7–0.1, which may rule out these explosion scenarios as the origin of this SNR. We note that our spectral data below 1 keV, where Fe L lines fall,

are missing due to the strong absorption, leaving the possibility that a significant amount of Fe is mixing into the IME-rich layer. Unless this is the case, our results prefer the carbon detonation model for the origin of G344.7–0.1.

We have also found that the peak location of the Fe emission (and thus the centroid of the IME arc) is offset to the west by $\sim 1'.6$ (corresponding to ~ 2.8 pc at the distance of 6 kpc) with respect to the geometric center of the SNR. This implies that either the SN explosion was asymmetric, or the Fe K peak location is the actual explosion center but an apparent asymmetry has formed during the SNR evolution. The spatial distribution of the plasma conditions may help disentangle this degeneracy. In particular, the ionization state of the Fe ejecta that is inferred from the Fe K centroid energy offers a useful diagnostic of the time duration since the ejecta were heated by the reverse shock (e.g. [Badenes et al. 2006](#); [Yamaguchi et al. 2014b](#)). Figure 6(a) shows the Fe K centroid energy observed in each region as a function of the angular distance from the location of the Fe emission, which reveals a positive correlation between the two quantities. The mean values of the centroid energy in the Fe peak and Si arc regions correspond to the charge states of Fe^{10+} and Fe^{17+} , respectively. Similarly, Table 4 indicates that a lower ionization timescale is achieved in the Fe peak region than in the outer regions. This suggests that the Fe ejecta at the inner regions were heated by the reverse shock more recently. We also plot in Figure 6(b) the electron temperatures of the NEI component of each region. In contrast to the Fe K centroid, the temperature is anticorrelated with the distance from the Fe peak location. We thus conclude that the location of the Fe peak region is the true explosion center of this SNR. The origin of the asymmetric morphology is discussed in more detail in §4.2.

One caveat is that the variation in the Fe K centroids may also be contributed by the line-of-sight velocity of the Fe ejecta, as was claimed for the Kepler SNR ([Kasuga et al. 2018](#)). We find that the observed variation in the Fe K centroid (~ 50 eV) requires a line-of-sight velocity v_{slight} of 2400 km s^{-1} for the Fe ejecta at the Fe peak region. If the Fe ejecta of the Fe peak location have been freely expanding for 3000 yr with $v_{\text{slight}} \sim 2400 \text{ km s}^{-1}$, the ejecta reach 7.4 pc from the SN explosion center, larger than the radius of this SNR (5 pc; assuming a distance of 6 kpc). Given that the ejecta must have been decelerated by the reverse shock, we should take this estimate as a lower limit. Since an unnaturally large asymmetry in the explosion is required to explain this line shift solely with the Doppler effect, the ionization effect is likely to be dominant in the observed variation in the Fe K centroid energies. The degeneracy between the ionization effect and Doppler shift in the Fe K emission can be disentangled by measurement of the $\text{Fe K}\beta/\text{K}\alpha$ flux ratio that strongly depends on the dominant charge state and thus

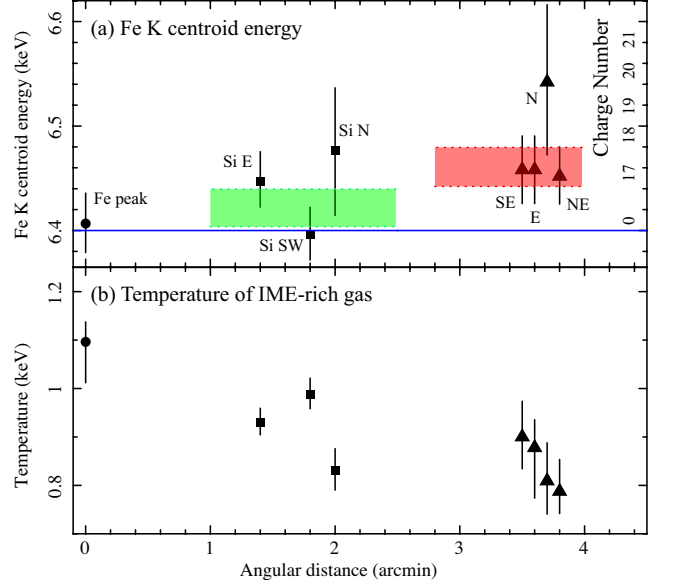


Figure 6. (a) Fe K centroid energy as a function of the radial distance from the Fe peak location. The corresponding charge number of Fe ions is given on the right. Green and red areas represent the values constrained by analyzing spectra from larger regions containing the entire Si arc (where square plots of Si E, SW, and N are all merged) and the entire rim regions (where triangle plots of SE, E, N, and NE are all merged), respectively. The blue solid line indicates the 6.40 keV level that corresponds to neutral Fe. (b) Electron temperature for the IME-rich gas component as a function of the radial distance from the Fe peak location. Square plots are the merged Si-arc region, and the triangle ones are the rim region.

constrains the rest-frame Fe K centroid ([Yamaguchi et al. 2014a](#)). Unfortunately, neither our Chandra observation nor any previous work allows us to detect Fe $\text{K}\beta$ emission due to poor photon statistics and limited energy resolution. Future high-resolution spectroscopy with XRISM and Athena are crucial to determine both charge state and line-of-sight velocity accurately.

Now we estimate the three-dimensional distribution of the v_{nei} component that is dominated by the IME ejecta, assuming that the Fe peak region is the true explosion center. Since the surface-brightness profiles of Si, S, Ar, and Ca (Figure 3) are virtually identical with one another, we use a radial profile of the 1.5–5.0 keV emission as representative of the IME distribution. Figure 7(a) shows the extracted radial profile compared with a simple two-zone spherical model assuming a uniform density and uniform abundance distribution in each zone. We also take into account the temperature gradient, and thus the emissivity variation, between the two zones, where ~ 1.1 keV at $< 1'$ and ~ 0.9 keV at $1'–3'$. Figure 7(b) shows the continuum-subtracted surface brightness of the Fe K and 1.5–5.0-keV emission, suggesting an

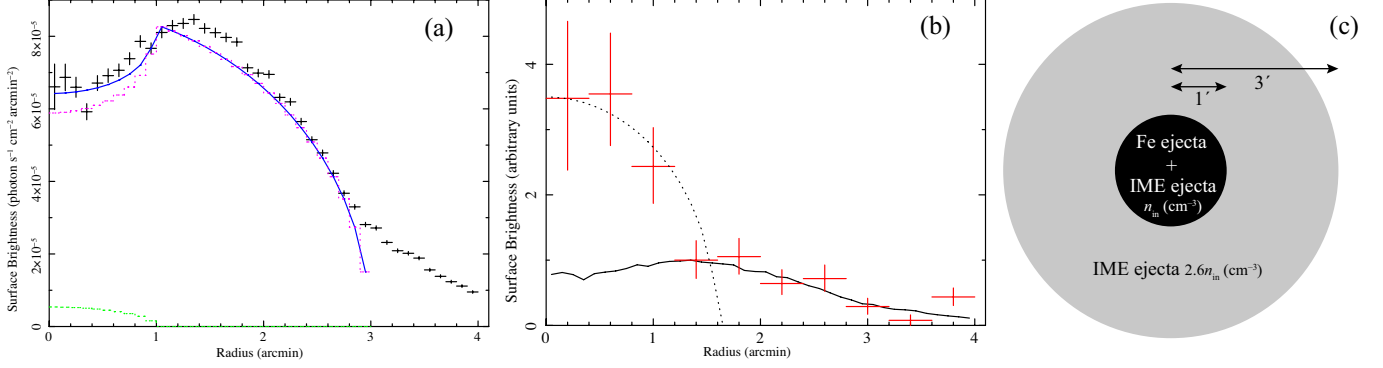


Figure 7. (a) Radial profile of the surface brightness in the IME band (1.5–5.0 keV), where the Fe peak position is assumed to be the SNR center. The blue solid line shows the modeled surface brightness that assumes a low-density inner sphere with a radius of $1'$ and a thick high-density shell with inner and outer radii of $1'$ and $3'$, respectively (see the text for more details). The density ratios of the outer shell to the inner sphere are assumed to be $n_{\text{shell}}/n_{\text{in}} = 2.6$. The magenta and green dashed lines show the contribution of the outer shell and inner sphere components to the total surface brightness, respectively. (b) Linearly scaled radial profiles of (a) and of surface brightness in the Fe K emission band. The solid line is for the scaled surface brightness of (a), and the red crosses for Fe K emission. The dotted line represents the modeled surface brightness assuming a spherical distribution of Fe ejecta. The continuum-subtracted flux of Fe K emission is determined by fitting with the model in §3.2. (c) Schematic view of the density distribution of G344.7–0.1 indicated in (a) and (b).

enhanced density of Fe ejecta at $< 1'$. We find that the observed profile is well reproduced by a model schematized in Figure 7(c): a low-density (n_{in}) inner sphere with a radius of $1'$ and a thick high-density ($n_{\text{shell}} = 2.6n_{\text{in}}$) shell with inner and outer radii of $1'$ and $3'$, respectively. The IME arc structure found in Figure 2(c) corresponds to the inner part of the thick shell, where the highest surface brightness is achieved. Note that the angular distance between the explosion center and the west rim is $\sim 3'$, and thus the excess in the brightness beyond this radius (Figure 7a) is solely due to the emission extended to the northeast.

4.2. Asymmetry

As discussed in the previous section, the identified explosion center is offset from the geometric center of the SNR. Therefore, the X-ray morphology of G344.7–0.1 is relatively asymmetric. Lopez et al. (2011) classified this SNR as a possible CC SNR because of such highly asymmetric X-ray morphology, based on the analysis of the power-ratio method (PRM). However, the dataset used in Lopez et al. (2011) has more limited photon statistics than our 200 ks Chandra data. Thus, we apply the PRM on our new dataset of G344.7–0.1 to measure the asymmetry of this SNR. We replicate the analysis from Lopez et al. (2011), where the PRs are calculated on the 0.5–2.1 keV band exposure-corrected image of SNR, and obtain $P_2/P_0 = 9.84^{+2.05}_{-2.32}$, $P_3/P_0 = 1.75^{+0.55}_{-0.62}$. The values are now comparable with those for the other well-

established Type Ia SNRs, such as Kepler. We note that the surface-brightness-weighted geometric center, i.e. the aperture center for the PRM, is $(\alpha_{J2000}, \delta_{J2000}) = (17^{\text{h}}03^{\text{m}}55^{\text{s}}.5, -41^{\circ}42'54''.5)$, which is almost the same as the geometric center of the SNR, and thus is offset from our proposed explosion center of $(\alpha_{J2000}, \delta_{J2000}) = (17^{\text{h}}03^{\text{m}}49^{\text{s}}.1, -41^{\circ}42'46''.0)$. This offset and apparent asymmetry seems to be caused by the nonuniform distribution of the ambient medium. In fact, other SNRs expanding in such ambient medium distributions (e.g., Kepler, N103B) also show high asymmetric morphology and off-center aperture center like G344.7–0.1 (Lopez et al. 2011).

The nonuniform density structure of the ambient medium is indeed found in our radio data. Figure 8 shows the total interstellar proton column density map $N_{\text{p}}(\text{H}_2 + \text{HI})$ combining both the molecular (CO: NANTEN2) and atomic (HI: McClure-Griffiths et al. 2005) components. The details of the radio observations and data analysis are described in Appendix B. The velocity range of the gas density map is from -118.0 km s^{-1} to -109.0 km s^{-1} , which corresponds to the kinematic distance of 6.2–6.4 kpc adopting a model of the Galactic rotation curve by Brand & Blitz (1993). The velocity range is determined by CO/HI cavities in the position-velocity diagrams (see Appendix B.3), suggesting an expanding gas motion originated by accretion winds from the progenitor system of the SNR (e.g., Sano et al. 2017, 2018). Therefore, the molecular and atomic clouds at the velocity range are likely associated with the SNR. The velocity range and distance to the SNR are consistent with the previous HI study by Giacani et al. (2011).

⁴ High P_2/P_0 indicates elliptical or elongated morphology, and high P_3/P_0 indicates asymmetric or nonuniform surface-brightness distribution (Lopez et al. 2011).

We find denser clouds possibly interacting with the SNR in the west (Figure 8), consistent with the previous results from the Mopra Southern Galactic Plane CO Survey (Burton et al. 2013; Braiding et al. 2015; Lau et al. 2019). The SNR expansion is likely to be decelerated by this interaction toward the west, resulting in the asymmetric morphology we observe. This interpretation is supported by the temperature gradient inferred from the mean energy map (Figure 2b); the lower temperature is achieved in the northeast region probably due to more efficient adiabatic expansion. A similar temperature gradient due to the asymmetric ambient density distribution is observed in other middle-aged SNRs, e.g., W49B (Lopez et al. 2013; Yamaguchi et al. 2018). Alternatively, the SN ejecta at the west could have been reheated by reflection shocks originating from the interaction with the dense clouds, as was observed in, for instance, Kes 27 (Chen et al. 2008).

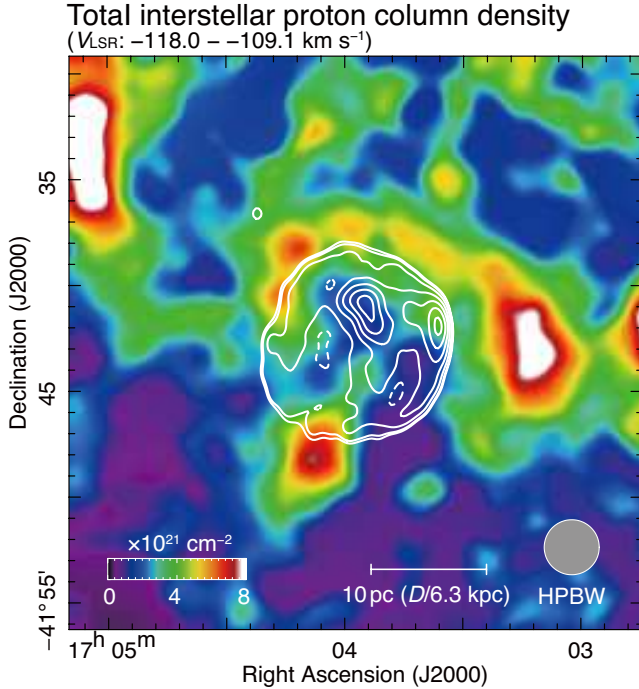


Figure 8. Map of total proton column density toward G344.7-0.1. The integration velocity range is from -118.0 km s^{-1} to -109.1 km s^{-1} , corresponding to the distance of $\sim 6.3 \text{ kpc}$. The half-power beamwidth is shown by field circle. The scale bar is calculated by assuming the distance of 6.3 kpc . The white contours indicate a 843 MHz radio continuum obtained with MOST (Whiteoak & Green 1996). The contour levels are 10.0, 12.5, 20.0, 32.5, 50.0, 72.5, and $100.0 \text{ mJy beam}^{-1}$.

We have also discovered a local asymmetric structure at the west rim, “Filament” in Figure 2(c). Interestingly, the measured IME abundances are enhanced with respect to the

solar values. Moreover, the relative abundances of S, Ar, Ca to Si are comparable to the solar composition and that of Mg is substantially lower, which is consistent with the typical nucleosynthesis yields of the incomplete Si burning (e.g., Iwamoto et al. 1999; Seitzzahl et al. 2013; Townsley et al. 2016). This implies an ejecta origin of this structure, despite that its filamentary morphology and location being more consistent with an interpretation of the forward shock front that propagates into the ISM. If the structure is indeed dominated by the SN ejecta, it is reminiscent of the ejecta knots in Tycho SNR, suggesting that such local asymmetry is somewhat common in a certain type of Type Ia SNRs.

4.3. Point-Like Sources

We have analyzed the spectra of the point-like sources detected with the total photon counts of 30 or more (see Table 2). The best-fit parameters for the absorbed blackbody model are given in Table 6, where the angular distance from the explosion center to the sources is given as well. If the sources are physically associated with the SNR, the measured absorption column density must be consistent with that of the SNR ($5-7 \times 10^{22} \text{ cm}^{-2}$). We find that only eight sources, No. 31, 36, 39, 41, 42, 43, 48, and 49, satisfy this criterion, and the other sources are most likely either foreground or background objects.

Next, we compare the temperature and luminosity of these sources with typical values for CCOs: $kT_{\text{bb}} = 0.2-0.5 \text{ keV}$ and $10^{33-34} \text{ erg s}^{-1}$ (e.g. Pavlov et al. 2004; Gotthelf et al. 2013). We find that four sources, No. 31, 36, 43 and 48 show typical kT_{bb} and luminosity as CCOs. These sources, however, have relatively large errors of 37–90% in N_{H} . Thus, we allow their N_{H} values to vary in the error ranges of N_{H} for the corresponding regions in Table 3 for each source. We finally find that all these four sources have low luminosities with expected N_{H} values of the different SNR regions. Therefore we conclude that there is no CCO associated with G344.7-0.1.

5. CONCLUSIONS

The elemental distribution in SNRs is the key to understanding the explosion mechanism of SNe. We have presented the results of the deep Chandra observations of the Type Ia SNR G344.7-0.1 revealed the distribution of the SN ejecta. The X-ray images and radial profiles of the surface brightness have revealed a centrally peaked distribution of the Fe ejecta, surrounded by an arc-like structure of the IMEs. The centroid energy of the Fe K emission is lower in the central Fe-rich region than in the outer IME-rich regions, suggesting that the Fe ejecta were heated by the reverse shock more recently in the IME regions. These results are consistent with predictions of standard SN Ia models, where the heavier elements are synthesized in the interior of an exploding white dwarf.

Table 6. Spectral Properties of All Point Sources

No. ^a	N_{H} (10^{22} cm $^{-2}$)	kT_{bb} (keV)	Luminosity ^b (10^{33} erg s $^{-1}$)	Distance (arcmin) ^c
1	< 0.06	$0.24^{+0.02}_{-0.01}$	$4.85^{+0.93}_{-0.47} \times 10^{-2}$	1.66
2	< 0.16	$0.43^{+0.03}_{-0.03}$	$3.53^{+0.56}_{-0.32} \times 10^{-2}$	3.34
3	< 0.09	$0.58^{+0.06}_{-0.05}$	$2.58^{+0.39}_{-0.35} \times 10^{-2}$	3.99
6	< 0.10	$0.59^{+0.07}_{-0.07}$	$1.02^{+0.21}_{-0.16} \times 10^{-2}$	4.69
7	< 0.38	$0.28^{+0.10}_{-0.07}$	$1.46^{+1.81}_{-0.30} \times 10^{-2}$	4.45
8	< 0.10	$0.84^{+0.14}_{-0.15}$	$1.11^{+0.37}_{-0.29} \times 10^{-2}$	5.35
9	< 0.93	$0.16^{+0.04}_{-0.06}$	$1.86^{+12.3}_{-0.87} \times 10^{-2}$	2.93
11	1596^{+616}_{-1008}	< 0.24 ^d	< 3.15×10^{16}	5.11
14	< 0.38	$0.34^{+0.07}_{-0.08}$	$0.84^{+0.62}_{-0.17} \times 10^{-2}$	6.55
15	< 0.14	$0.48^{+0.05}_{-0.05}$	$3.23^{+0.61}_{-0.48} \times 10^{-2}$	6.33
16	< 0.68	$0.21^{+0.05}_{-0.04}$	$1.05^{+0.80}_{-0.38} \times 10^{-2}$	4.29
17	< 0.71	$0.54^{+0.08}_{-0.07}$	$4.08^{+1.01}_{-0.23} \times 10^{-2}$	2.66
18	< 2.45	$0.25^{+0.10}_{-0.14}$	$0.78^{+10.6}_{-0.37} \times 10^{-2}$	3.85
19	< 0.62	$0.45^{+0.17}_{-0.34}$	$0.23^{+0.24}_{-0.23} \times 10^{-2}$	3.09
20	< 0.25	$0.80^{+0.07}_{-0.08}$	$4.66^{+0.69}_{-0.60} \times 10^{-2}$	1.04
22	< 0.54	$0.39^{+0.10}_{-0.10}$	$1.05^{+0.81}_{-0.20} \times 10^{-2}$	4.38
24	< 1.23	$0.56^{+0.11}_{-0.16}$	$1.49^{+1.27}_{-0.36} \times 10^{-2}$	4.17
25	< 0.41	$0.88^{+0.44}_{-0.31}$	$0.74^{+0.44}_{-0.28} \times 10^{-2}$	4.82
26	$2.65^{+1.54}_{-1.20}$	$0.79^{+0.17}_{-0.13}$	$4.05^{+1.52}_{-0.90} \times 10^{-2}$	3.03
27	$38^{+0.8}_{-4.7}$	$2.73^{+0.14}_{-0.02} \times 10^{-2}$	< 3.60×10^{29}	2.63
28	< 0.62	$0.48^{+0.15}_{-0.14}$	$0.51^{+0.31}_{-0.17} \times 10^{-2}$	4.58
29	< 1.90	> 2.26	< 253	6.82
30	< 0.39	$0.90^{+0.27}_{-0.19}$	$0.66^{+0.38}_{-0.35} \times 10^{-2}$	3.96
31	$7.44^{+5.60}_{-3.29}$	$0.37^{+0.13}_{-0.11}$	< 2.77	1.51
	6.69^e	$0.39^{+0.05}_{-0.04}$	$0.21^{+0.09}_{-0.08}$	
32	$8.66^{+7.79}_{-3.38}$	< 0.18	< 7.64×10^{10}	1.74
33	38^{+23}_{-14}	$0.07^{+0.04}_{-0.02}$	< 9.00×10^{11}	3.17
34	$2.42^{+1.19}_{-0.89}$	$0.62^{+0.09}_{-0.08}$	$0.12^{+0.05}_{-0.03}$	2.89
35	> 710	< 197	< 5.36×10^7	1.83
36	$6.74^{+3.17}_{-2.49}$	$0.35^{+0.09}_{-0.07}$	< 1.12	2.93
	6.63^e	$0.35^{+0.06}_{-0.03}$	$0.24^{+0.10}_{-0.13}$	
37	$2.18^{+1.90}_{-1.29}$	$0.63^{+0.20}_{-0.14}$	$3.27^{+2.96}_{-1.18} \times 10^{-2}$	1.52
38	27^{+19}_{-13}	$0.12^{+0.07}_{-0.04}$	< 4.12×10^5	1.45
39	$3.60^{+2.73}_{-1.78}$	$0.49^{+0.14}_{-0.12}$	$5.67^{+12.1}_{-2.97} \times 10^{-2}$	2.80
41	< 28.3	< 4.19	$1.01^{+8.50}_{-0.55} \times 10^{-2}$	1.33
42	$3.27^{+6.25}_{-3.11}$	$0.67^{+0.44}_{-0.32}$	$1.06^{+8.65}_{-0.64} \times 10^{-2}$	0.97
43	$4.31^{+2.90}_{-2.00}$	$0.34^{+0.13}_{-0.10}$	< 1.47	2.29
	4.76^e	$0.33^{+0.04}_{-0.09}$	$0.25^{+0.72}_{-0.07}$	
45	77^{+21}_{-17}	$3.87^{+4.57}_{-3.57} \times 10^{-2}$	< 3.60×10^{29}	1.97
46	122^{+16}_{-34}	< 0.06	< 416	2.12
47	$2.25^{+1.80}_{-1.41}$	$0.50^{+0.18}_{-0.15}$	$2.93^{+5.54}_{-1.58} \times 10^{-2}$	2.50
48	$7.80^{+6.99}_{-3.60}$	$0.29^{+0.14}_{-0.13}$	< 5.13	4.94
	6.50^e	$0.33^{+0.05}_{-0.04}$	$0.19^{+0.12}_{-0.10}$	
49	< 11	$0.52^{+0.99}_{-0.18}$	< 0.37	4.22

^aFaint sources are excluded (see §3.1).^bWe assume the distance to the SNR to be 6 kpc.^cThe angular distance from the Fe peak location.^dWe allow kT_{bb} to vary in 0.2–0.5 keV for this source.^eBest-fit values applied constraints in error ranges on each corresponding SNR region in Table 3.

This work is financially supported by the *Chandra* GO Program grant GO8-19052A and Grants-in-Aid for Scientific Research (KAKENHI) of the Japanese Society for the Promotion of Science (JSPS) grants No., 19H00704 (HY), and 24224005 and 19H05075 (HS). S.K. is supported by the Leading Initiative for Excellent Young Researchers, Ministry of Education, Culture, Sports, Science and Technology (MEXT), Japan. H.S. is supported by “Building of Consortium for the Development of Human Resources in Science and Technology” of MEXT (grant No. 01-M1-0305). NANTEN2

is an international collaboration of 11 universities: Nagoya University, Osaka Prefecture University, University of Bonn, University of Cologne, Seoul National University, University of Chile, University of New South Wales, Macquarie University, University of Sydney, University of Adelaide, and University of ETH Zurich.

Software: CIAO (Fruscione et al. 2006), XSPEC (Arnaud 1996)

APPENDIX

A. BACKGROUND ESTIMATION

An X-ray background consists of three major components, non X-ray background (NXB), cosmic X-ray background (CXB), and the Galactic thermal emission. The third component is non-negligible in our study, since G344.7–0.1 is located in the Galactic plane.

Table 7. Best-fit Parameters for the Background Model

Components	Parameters	
NXB	Γ_1	$0.32^{+0.01}_{-0.01}$
	Γ_2	$-0.78^{+0.04}_{-0.04}$
	E_{break} (keV)	$5.32^{+0.11}_{-0.13}$
	K_{NXB}^c	$5.68^{+0.06}_{-0.06} \times 10^{-2}$
Absorption ^a	N_{H} (10^{22} cm^{-2})	$7.34^{+0.25}_{-0.26}$
CXB	Γ	1.40 (fix)
	K_{CXB}^c	5.65×10^{-5} (fix)
Galactic thermal emissions ^b	kT_{apec1} (keV)	$0.35^{+0.02}_{-0.02}$
	VEM ^d	$0.26^{+0.06}_{-0.05}$
	kT_{apec2} (keV)	$0.79^{+0.17}_{-0.18}$
	VEM ^d	$4.76^{+8.71}_{-4.28} \times 10^{-3}$
C-statistic/dof		1410.75/1152

^aThe absorption cross sections are taken from Verner et al. (1996).

^bSolar abundances of Wilms et al. (2000) are assumed.

^cIn units of photon $\text{keV}^{-1} \text{ cm}^{-2} \text{ s}^{-1}$ at 1 keV.

^dIn units of 10^{14} cm^{-5} . The volume emission measure (VEM) is given as $\int n_e n_H dV / (4\pi D^2)$, where V and D are the volume of the emission region (cm^3) and the distance to the emitting source (cm), respectively.

The NXB spectra contain several fluorescence lines and continuum emission. We reproduce the NXB component with a model of the `bknpowerlaw` + 5 Gaussians. Gaussians are for instrumental emission lines of Al $K\alpha$ ($\sim 1.47 \text{ keV}$), Au $M\alpha$ ($\sim 2.11 \text{ keV}$), Au $M\beta$

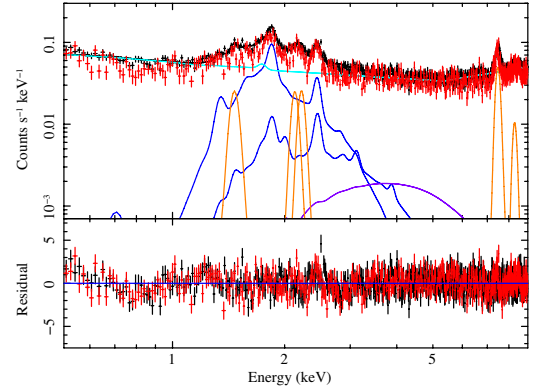


Figure 9. Raw spectra of the background region around G344.7–0.1. The black and red data are the data from the May and July observation series, respectively. The solid lines represent the following models for the spectrum taken in 2018 May, black: best-fit model; light blue: NXB continuum; orange: instrumental emission lines; blue: Galactic thermal emissions; and purple: CXB.

($\sim 2.20 \text{ keV}$), Ni $K\alpha$ ($\sim 7.47 \text{ keV}$), and Ni $K\beta$ ($\sim 8.29 \text{ keV}$). We assume `tbnew_gas` \times `powerlaw` model for the CXB emission. The typical value of CXB normalization is $N_{\text{CXB}} \sim 8\text{--}10 \text{ photon keV}^{-1} \text{ cm}^{-2} \text{ s}^{-1} \text{ sr}^{-1}$ at 1 keV (Nakashima et al. 2018, Suzaku). The solid angle of our background region is $(7^2 - 5^2)\pi \text{ arcmin}^2 \sim 6.28 \times 10^{-6} \text{ sr}$, so we estimate the CXB normalization $K_{\text{CXB}} = 5.65 \times 10^{-5} \text{ photon keV}^{-1} \text{ cm}^{-2} \text{ s}^{-1}$ at 1 keV. We fix $\Gamma = 1.40$ and $K_{\text{CXB}} = 5.65 \times 10^{-5} \text{ photon keV}^{-1} \text{ cm}^{-2} \text{ s}^{-1}$ at 1 keV for the CXB `powerlaw`. For the final component, Galactic thermal emissions, which are dominant in the 1–5 keV band, we use two absorbed APEC models, as `tbnew_gas` \times (`apec+apec`). Metal abundances of the APEC components are assumed to be the solar value of Wilms et al. (2000). We link the absorption column density N_{H} to that of the CXB. Table 7 gives the best-fit parameters of our background model. This best-fit model is shown in Figure 9.

The intensities of the Galactic center X-ray emission (GCXE) and Galactic ridge X-ray emission (GRXE) are modeled by Uchiyama et al. (2013) based on many *Suzaku* observations. We compared the intensity of the Galactic emission component in our model with the predictions of the GCXE and GRXE intensities in this paper. We calculated the intensity in the 2.3–5.0 keV band based on equation (1) in Uchiyama et al. (2013) and derived a value of $12.6 \times 10^{-7} \text{ photons s}^{-1} \text{ cm}^{-2} \text{ arcmin}^{-2}$ which compares with the value in our model of $12.1^{+4.2}_{-9.3} \times 10^{-7} \text{ photons s}^{-1} \text{ cm}^{-2} \text{ arcmin}^{-2}$ (within 90% errors). Therefore, our model intensity for the Galactic emission is consistent with the model predictions in Uchiyama et al. (2013).

B. RADIO OBSERVATIONS

B.1. CO and HI

Observations of ^{12}CO ($J=1-0$) line emission at 115.271202 GHz were executed in 2012 May 18th using the NANTEN2 millimeter/submillimeter radio telescope. The telescope is installed at 4865 m altitude of the Atacama Desert in Chile, operated by Nagoya University. We observed an area of $1^\circ \times 1^\circ$ region using the on-the-fly mapping mode with Nyquist sampling. The 4 K cooled Nb superconductor-insulator-superconductor mixer receiver was used for the front end. The system temperature including the atmosphere was ~ 200 K in the double-side band. The backend was a digital Fourier-transform spectrometer with 1684 channels or 1 GHz bandwidth, corresponding to a velocity coverage of 2600 km s^{-1} and a velocity resolution of 0.16 km s^{-1} . After convolving the cube data with a two-dimensional Gaussian kernel of $90''$, the final beam size was $\sim 180''$ in FWHM. The absolute intensity was calibrated by observing the standard source IRAS 16293–2422 [$(\alpha_{J2000}, \delta_{J2000}) = (16^{\text{h}}32^{\text{m}}23^{\text{s}}.3, -24^\circ28'39''.2)$] (Ridge et al. 2006). We also observed IRC+10216 every day, and the pointing accuracy was better than $10''$. The typical noise fluctuation of the final dataset is ~ 0.65 K at the velocity resolution of 0.63 km s^{-1} .

The HI line data at 1.4 GHz is from the Southern Galactic Plane Survey (SGPS; McClure-Griffiths et al. 2005). The archival dataset was obtained using a combination of the Australia Telescope Compact Array (ATCA) and Parkes radio telescope. The angular resolution is $130''$ and the velocity resolution is 0.82 km s^{-1} . The typical noise fluctuation is ~ 1.9 K at the velocity resolution of 0.82 km s^{-1} .

B.2. Estimation of Total ISM Protons

To obtain the total proton column density map, we estimate proton column densities in both the molecular and atomic clouds (e.g., Fukui et al. 2012, 2017; Kuriki et al. 2018; Sano et al. 2019). The proton column density of

molecular cloud $N_{\text{p}}(\text{H}_2)$ can be estimated from the following equations:

$$\begin{aligned} N(\text{H}_2) &= X_{\text{CO}} \cdot W(\text{CO}) \text{ (cm}^{-2}\text{)} \\ N_{\text{p}}(\text{H}_2) &= 2 \times N(\text{H}_2) \text{ (cm}^{-2}\text{)} \end{aligned}$$

where $N(\text{H}_2)$ is the column density of molecular hydrogen in units of cm^{-2} , X_{CO} is the CO-to- H_2 conversion factor in units of $(\text{K km s}^{-1})^{-1} \text{ cm}^{-2}$, and $W(\text{CO})$ is the integrated intensity of CO in units of K km s^{-1} . In the present paper, we used $X_{\text{CO}} = 2.0 \times 10^{20} (\text{K km s}^{-1})^{-1} \text{ cm}^{-2}$ (Bertsch et al. 1993).

On the other hand, an estimation of the proton column density of atomic cloud $N_{\text{p}}(\text{HI})$ is tricky because we should consider the optical depth of HI. According to Fukui et al. (2015), 91% of atomic hydrogen in local clouds has an optical depth of 0.5 or higher with respect to the HI line emission. Therefore we cannot use the well-known equation assuming the optical depth of HI $\ll 1$ (e.g., Dickey & Lockman 1990):

$$N_{\text{p}}(\text{HI}) = 1.823 \times 10^{18} W(\text{HI}) \text{ (cm}^{-2}\text{)}$$

where $W(\text{HI})$ is the integrated intensity of HI in units of K km s^{-1} .

To estimate the optical-depth-corrected proton column density of atomic cloud $N_{\text{p}}(\text{HI})'$, we used a relation between $W(\text{HI})$ and $N_{\text{p}}(\text{HI})'$ presented by Fukui et al. (2017). The authors derived $N_{\text{p}}(\text{HI})'$ as a function of $W(\text{HI})$ using the dust opacity map at 353 GHz obtained from IRAS and Planck datasets (Planck Collaboration et al. 2014) taking into account nonlinear dust properties (e.g., Roy et al. 2013; Okamoto et al. 2017; Hayashi et al. 2019a,b). In the present paper, we derived a conversion factor from $W(\text{HI})$ to $N_{\text{p}}(\text{HI})'$ fitted by the result of Fukui et al. (2017) as a function of $W(\text{HI})$. We obtained averaged value of $N_{\text{p}}(\text{HI})'$ toward G344.7–0.1 is $\sim 1.2 \times 10^{21} \text{ cm}^{-2}$, which is ~ 2.3 times higher than that of $N_{\text{p}}(\text{HI})$ assuming the optically thin case. Finally, we derived the total proton column density map $N_{\text{p}}(\text{H}_2 + \text{HI})$ combining $N_{\text{p}}(\text{HI})'$ and $N_{\text{p}}(\text{H}_2)$ whose angular resolution is smoothed to match the FWHM of NANTEN2 beam size of $\sim 180''$ (see Figure 8).

B.3. An Expanding Gas Motion

Giacani et al. (2011) argued that G344.7–0.1 is likely associated with an open HI shell at the central velocity of $\sim 115 \text{ km s}^{-1}$, corresponding to the kinematic distance of 6.3 ± 0.1 kpc. Here, we investigate the cloud association by using both the CO and HI datasets.

Figures 10(a) and 10(c) show the integrated intensity maps of HI and CO at a velocity of $\sim 115 \text{ km s}^{-1}$, respectively. We found a presence of shell-like structure not only in the HI map, but also in the CO map. The CO clouds nicely surround the SNR, especially for the northern half of the shell.

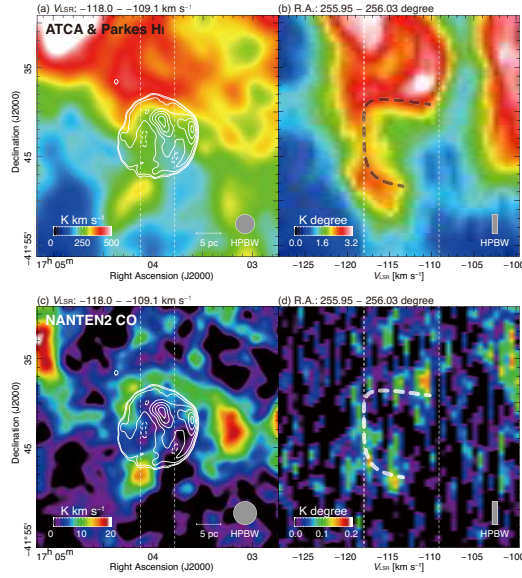


Figure 10. (a), (c) Integrated intensity map of (a) HI and (c) CO superposed on the MOST 843 MHz radio continuum. The integration velocity range and contour levels are the same as in Figure 8. The scale bars at a distance of 6.3 kpc and half-power beamwidths are also shown in the bottom right corner. The dashed vertical lines indicate the integration range of the position-velocity diagram in the Figures 10(b) and 10(d). (b), (d) Position-velocity diagrams of (b) HI and (d) CO. The integration range in R.A. is from $255^{\circ}.95$ to $256^{\circ}.03$. The beam size and velocity resolution of each map are shown in the bottom right corner. The dashed curves indicate a boundary of the CO or HI cavity in the position-velocity diagram (see the text).

Figures 10(b) and 10(d) show the position-velocity diagrams of HI and CO, respectively. We found cavity-like structures of HI and CO (dashed lines) in the velocity range from -118.0 km s^{-1} to -109.1 km s^{-1} , which have a similar diameter to G344.7–0.1 in terms of the decl. These cavity-like structures represent an expanding gas motion similar to a “wind-blown shell,” originated by strong winds from the progenitor system: e.g., stellar winds from a high-mass progenitor or accretion winds (also known as “disk winds”) from a single degenerate progenitor system of Type Ia SNR. For the case of Type Ia SNR G344.7–0.1, the latter origin is favored. The expansion velocity of molecular and atomic clouds ΔV is estimated to be $\sim 4.5 \text{ km s}^{-1}$, which is consistent with the previous studies of interstellar environments in the Type Ia SNRs (e.g., *Tycho*, $\Delta V \sim 4.5 \text{ km s}^{-1}$, Zhou et al. 2016; N103B, $\Delta V \sim 5 \text{ km s}^{-1}$, Sano et al. 2018). In any case, the SNR shock wave travels through the wind-blown shell during the free expansion phase, and is finally decelerated when the shockwave encounters the wind wall. Therefore, the size of the SNR generally coincides with that of the wind-blown shell. Summarizing the above considerations, both the molecular and atomic clouds in the velocity range from -118.0 km s^{-1} to -109.1 km s^{-1} are likely associated with the SNR G344.7–0.1, which is consistent with the previous HI study by Giacani et al. (2011).

REFERENCES

- Anders, E., & Grevesse, N. 1989, *GeoCoA*, 53, 197, doi: [10.1016/0016-7037\(89\)90286-X](https://doi.org/10.1016/0016-7037(89)90286-X)
- Arnaud, K. A. 1996, in *Astronomical Society of the Pacific Conference Series*, Vol. 101, *Astronomical Data Analysis Software and Systems V*, ed. G. H. Jacoby & J. Barnes, 17
- Badenes, C., Borkowski, K. J., Hughes, J. P., Hwang, U., & Bravo, E. 2006, *ApJ*, 645, 1373, doi: [10.1086/504399](https://doi.org/10.1086/504399)
- Bertsch, D. L., Dame, T. M., Fichtel, C. E., et al. 1993, *ApJ*, 416, 587, doi: [10.1086/173261](https://doi.org/10.1086/173261)
- Braiding, C., Burton, M. G., Blackwell, R., et al. 2015, *PASA*, 32, e020, doi: [10.1017/pasa.2015.20](https://doi.org/10.1017/pasa.2015.20)
- Brand, J., & Blitz, L. 1993, *A&A*, 275, 67
- Burton, M. G., Braiding, C., Glueck, C., et al. 2013, *PASA*, 30, e044, doi: [10.1017/pasa.2013.22](https://doi.org/10.1017/pasa.2013.22)
- Cash, W. 1979, *ApJ*, 228, 939, doi: [10.1086/156922](https://doi.org/10.1086/156922)
- Chen, Y., Seward, F. D., Sun, M., & Li, J.-t. 2008, *ApJ*, 676, 1040, doi: [10.1086/525240](https://doi.org/10.1086/525240)
- Clark, D. H., Caswell, J. L., & Green, A. J. 1975, *Australian Journal of Physics Astrophysical Supplement*, 37, 1
- Combi, J. A., Albacete Colombo, J. F., López-Santiago, J., et al. 2010, *A&A*, 522, A50, doi: [10.1051/0004-6361/200913735](https://doi.org/10.1051/0004-6361/200913735)
- David, L. P., Jones, C., Forman, W., et al. 2009, *ApJ*, 705, 624, doi: [10.1088/0004-637X/705/1/624](https://doi.org/10.1088/0004-637X/705/1/624)
- Decourchelle, A. 2017, *Supernova of 1572, Tycho’s Supernova*, 117, doi: [10.1007/978-3-319-21846-5_48](https://doi.org/10.1007/978-3-319-21846-5_48)
- Dickey, J. M., & Lockman, F. J. 1990, *ARA&A*, 28, 215, doi: [10.1146/annurev.aa.28.090190.001243](https://doi.org/10.1146/annurev.aa.28.090190.001243)
- Fink, M., Kromer, M., Seitenzahl, I. R., et al. 2014, *MNRAS*, 438, 1762, doi: [10.1093/mnras/stt2315](https://doi.org/10.1093/mnras/stt2315)
- Fruscione, A., McDowell, J. C., Allen, G. E., et al. 2006, in *Society of Photo-Optical Instrumentation Engineers (SPIE) Conference Series*, Vol. 6270, *Proc. SPIE*, 62701V, doi: [10.1117/12.671760](https://doi.org/10.1117/12.671760)
- Fukui, Y., Torii, K., Onishi, T., et al. 2015, *ApJ*, 798, 6, doi: [10.1088/0004-637X/798/1/6](https://doi.org/10.1088/0004-637X/798/1/6)

- Fukui, Y., Sano, H., Sato, J., et al. 2012, *ApJ*, 746, 82, doi: [10.1088/0004-637X/746/1/82](https://doi.org/10.1088/0004-637X/746/1/82)
- . 2017, *ApJ*, 850, 71, doi: [10.3847/1538-4357/aa9219](https://doi.org/10.3847/1538-4357/aa9219)
- Garmire, G. P., Bautz, M. W., Ford, P. G., Nousek, J. A., & Ricker, George R., J. 2003, in *Society of Photo-Optical Instrumentation Engineers (SPIE) Conference Series*, Vol. 4851, Proc. SPIE, ed. J. E. Truemper & H. D. Tananbaum, 28–44, doi: [10.1117/12.461599](https://doi.org/10.1117/12.461599)
- Giacani, E., Smith, M. J. S., Dubner, G., & Loiseau, N. 2011, *A&A*, 531, A138, doi: [10.1051/0004-6361/201116768](https://doi.org/10.1051/0004-6361/201116768)
- Gotthelf, E. V., Halpern, J. P., & Alford, J. 2013, *The Astrophysical Journal*, 765, 58, doi: [10.1088/0004-637X/765/1/58](https://doi.org/10.1088/0004-637X/765/1/58)
- Hayashi, K., Okamoto, R., Yamamoto, H., et al. 2019a, *ApJ*, 878, 131, doi: [10.3847/1538-4357/ab2051](https://doi.org/10.3847/1538-4357/ab2051)
- Hayashi, K., Mizuno, T., Fukui, Y., et al. 2019b, *ApJ*, 884, 130, doi: [10.3847/1538-4357/ab4351](https://doi.org/10.3847/1538-4357/ab4351)
- Hughes, J. P., Ghavamian, P., Rakowski, C. E., & Slane, P. O. 2003, *ApJL*, 582, L95, doi: [10.1086/367760](https://doi.org/10.1086/367760)
- Iwamoto, K., Brachwitz, F., Nomoto, K., et al. 1999, *ApJS*, 125, 439, doi: [10.1086/313278](https://doi.org/10.1086/313278)
- Kasuga, T., Sato, T., Mori, K., Yamaguchi, H., & Bamba, A. 2018, *PASJ*, 70, 88, doi: [10.1093/pasj/psy085](https://doi.org/10.1093/pasj/psy085)
- Katsuda, S. 2017, *Supernova of 1006 (G327.6+14.6)*, 63, doi: [10.1007/978-3-319-21846-5_45](https://doi.org/10.1007/978-3-319-21846-5_45)
- Kuriki, M., Sano, H., Kuno, N., et al. 2018, *ApJ*, 864, 161, doi: [10.3847/1538-4357/aad7be](https://doi.org/10.3847/1538-4357/aad7be)
- Lau, J. C., Rowell, G., Voisin, F., et al. 2019, *MNRAS*, 483, 3659, doi: [10.1093/mnras/sty3326](https://doi.org/10.1093/mnras/sty3326)
- Lopez, L. A., Pearson, S., Ramirez-Ruiz, E., et al. 2013, *ApJ*, 777, 145, doi: [10.1088/0004-637X/777/2/145](https://doi.org/10.1088/0004-637X/777/2/145)
- Lopez, L. A., Ramirez-Ruiz, E., Huppenkothen, D., Badenes, C., & Pooley, D. A. 2011, *ApJ*, 732, 114, doi: [10.1088/0004-637X/732/2/114](https://doi.org/10.1088/0004-637X/732/2/114)
- McClure-Griffiths, N. M., Dickey, J. M., Gaensler, B. M., et al. 2005, *ApJS*, 158, 178, doi: [10.1086/430114](https://doi.org/10.1086/430114)
- Nakashima, S., Inoue, Y., Yamasaki, N., et al. 2018, *ApJ*, 862, 34, doi: [10.3847/1538-4357/aacceb](https://doi.org/10.3847/1538-4357/aacceb)
- Okamoto, R., Yamamoto, H., Tachihara, K., et al. 2017, *ApJ*, 838, 132, doi: [10.3847/1538-4357/aa6747](https://doi.org/10.3847/1538-4357/aa6747)
- Pavlov, G. G., Sanwal, D., & Teter, M. A. 2004, in *IAU Symposium*, Vol. 218, *Young Neutron Stars and Their Environments*, ed. F. Camilo & B. M. Gaensler, 239, <https://arxiv.org/abs/astro-ph/0311526>
- Perlmutter, S., Aldering, G., della Valle, M., et al. 1998, *Nature*, 391, 51, doi: [10.1038/34124](https://doi.org/10.1038/34124)
- Planck Collaboration, Abergel, A., Ade, P. A. R., et al. 2014, *A&A*, 571, A11, doi: [10.1051/0004-6361/201323195](https://doi.org/10.1051/0004-6361/201323195)
- Post, S., Park, S., Badenes, C., et al. 2014, *ApJL*, 792, L20, doi: [10.1088/2041-8205/792/1/L20](https://doi.org/10.1088/2041-8205/792/1/L20)
- Reddy, B. E., Lambert, D. L., & Allende Prieto, C. 2006, *MNRAS*, 367, 1329, doi: [10.1111/j.1365-2966.2006.10148.x](https://doi.org/10.1111/j.1365-2966.2006.10148.x)
- Ridge, N. A., Di Francesco, J., Kirk, H., et al. 2006, *AJ*, 131, 2921, doi: [10.1086/503704](https://doi.org/10.1086/503704)
- Riess, A. G., Filippenko, A. V., Challis, P., et al. 1998, *AJ*, 116, 1009, doi: [10.1086/300499](https://doi.org/10.1086/300499)
- Roy, A., Martin, P. G., Polychroni, D., et al. 2013, *ApJ*, 763, 55, doi: [10.1088/0004-637X/763/1/55](https://doi.org/10.1088/0004-637X/763/1/55)
- Sano, H., Reynoso, E. M., Mitsuishi, I., et al. 2017, *Journal of High Energy Astrophysics*, 15, 1, doi: [10.1016/j.jheap.2017.04.002](https://doi.org/10.1016/j.jheap.2017.04.002)
- Sano, H., Yamane, Y., Tokuda, K., et al. 2018, *ApJ*, 867, 7, doi: [10.3847/1538-4357/aae07c](https://doi.org/10.3847/1538-4357/aae07c)
- Sano, H., Rowell, G., Reynoso, E. M., et al. 2019, *ApJ*, 876, 37, doi: [10.3847/1538-4357/ab108f](https://doi.org/10.3847/1538-4357/ab108f)
- Sato, K., Tokoi, K., Matsushita, K., et al. 2007, *ApJL*, 667, L41, doi: [10.1086/522031](https://doi.org/10.1086/522031)
- Seitenzahl, I. R., Ciaraldi-Schoolmann, F., Röpke, F. K., et al. 2013, *MNRAS*, 429, 1156, doi: [10.1093/mnras/sts402](https://doi.org/10.1093/mnras/sts402)
- Sim, S. A., Fink, M., Kromer, M., et al. 2012, *MNRAS*, 420, 3003, doi: [10.1111/j.1365-2966.2011.20162.x](https://doi.org/10.1111/j.1365-2966.2011.20162.x)
- Sugizaki, M., Mitsuda, K., Kaneda, H., et al. 2001, *ApJS*, 134, 77, doi: [10.1086/320358](https://doi.org/10.1086/320358)
- Townsley, D. M., Miles, B. J., Timmes, F. X., Calder, A. C., & Brown, E. F. 2016, *ApJS*, 225, 3, doi: [10.3847/0067-0049/225/1/3](https://doi.org/10.3847/0067-0049/225/1/3)
- Troja, E., Bocchino, F., Miceli, M., & Reale, F. 2008, *A&A*, 485, 777, doi: [10.1051/0004-6361:20079123](https://doi.org/10.1051/0004-6361:20079123)
- Uchiyama, H., Nobukawa, M., Tsuru, T. G., & Koyama, K. 2013, *PASJ*, 65, 19, doi: [10.1093/pasj/65.1.19](https://doi.org/10.1093/pasj/65.1.19)
- Verner, D. A., Ferland, G. J., Korista, K. T., & Yakovlev, D. G. 1996, *ApJ*, 465, 487, doi: [10.1086/177435](https://doi.org/10.1086/177435)
- Vink, J. 2017, *Supernova 1604, Kepler's Supernova, and its Remnant*, 139, doi: [10.1007/978-3-319-21846-5_49](https://doi.org/10.1007/978-3-319-21846-5_49)
- Whiteoak, J. B. Z., & Green, A. J. 1996, *A&AS*, 118, 329
- Wilms, J., Allen, A., & McCray, R. 2000, *ApJ*, 542, 914, doi: [10.1086/317016](https://doi.org/10.1086/317016)
- Yamaguchi, H., Tanaka, M., Maeda, K., et al. 2012, *ApJ*, 749, 137, doi: [10.1088/0004-637X/749/2/137](https://doi.org/10.1088/0004-637X/749/2/137)
- Yamaguchi, H., Badenes, C., Petre, R., et al. 2014a, *ApJL*, 785, L27, doi: [10.1088/2041-8205/785/2/L27](https://doi.org/10.1088/2041-8205/785/2/L27)
- Yamaguchi, H., Eriksen, K. A., Badenes, C., et al. 2014b, *ApJ*, 780, 136, doi: [10.1088/0004-637X/780/2/136](https://doi.org/10.1088/0004-637X/780/2/136)
- Yamaguchi, H., Tanaka, T., Wik, D. R., et al. 2018, *ApJL*, 868, L35, doi: [10.3847/2041-8213/aaf055](https://doi.org/10.3847/2041-8213/aaf055)
- Yamauchi, S., Ueno, M., Koyama, K., & Bamba, A. 2005, *PASJ*, 57, 459, doi: [10.1093/pasj/57.3.459](https://doi.org/10.1093/pasj/57.3.459)
- Zhou, P., Chen, Y., Zhang, Z.-Y., et al. 2016, *ApJ*, 826, 34, doi: [10.3847/0004-637X/826/1/34](https://doi.org/10.3847/0004-637X/826/1/34)